Article:
Wang, S, Yu, X, Shen, L et al. (5 more authors) (2021) Noise reduction of automobile cooling fan based on bio-inspired design. Proceedings of the Institution of Mechanical Engineers, Part D: Journal of Automobile Engineering, 235 (2-3). pp. 465-478. ISSN 0954-4070

https://doi.org/10.1177/0954407020959892

Noise reduction of automobile cooling fan based on bio-inspired design

Shuwen Wang[a], Xinke Yu[a], Lixia Shen[a], Ailing Yang[b], Eryun Chen[b], John Fieldhouse[c], David Barton[c], Shahriar Kosarieh[c]

[a] College of Mechanical Engineering, University of Shanghai for Science and Technology, Shanghai 200093, China

[b] College of Energy and Power Engineering, University of Shanghai for Science and Technology, Shanghai 200093, China

[c] School of Mechanical Engineering, University of Leeds, LS2 9JT, United Kingdom

Abstract

This study aims to minimize the noise generated by automobile cooling fans. Fan blade structures with ridged surfaces based on bio-inspired principles are 3D printed and used to replace the conventional fan blades. The effect of the bio-inspired ridge structures on the noise reduction of the cooling fan is demonstrated by orthogonal experiments in a semi-anechoic chamber. Experimental results show that with an increase in the rotational speed, the effect of the surface textures on the acoustic performance of the cooling fan becomes more significant. For example, at a fan speed of 1750 r/min, all the bio-inspired blade designs reduce noise compared with the original fan and, in particular, the sound pressure level is reduced by 3.83 dB(A) for the design with a ridge width of 4 mm and a ridge pitch of 15 mm. Through variance

analysis of the measured noise, the ridge pitch distance has the most significant impact on noise reduction under low speed conditions whilst, under high speed conditions, the ridge width has the most significant influence. In addition to the experimental studies, computational fluid dynamics (CFD) simulations of the cooling fan are carried out to explain the mechanism of noise reduction for the ridged fan blades. When the fan runs, the horseshoe vortexes generated by the ridge structures disturb the flow of the boundary layer, reduce the influence of the fluid flow on the boundary layer, and delay the transition of the fan blade laminar flow to turbulence. It is also seen that there is a reduction of the intensity of the fan blade trailing edge vortices and the scale of the secondary vortices, thereby achieving the overall aim of noise reduction. This research has significance in the noise reduction design of automobile cooling fans.

Keywords: Automobile cooling fan, bio-inspired design, 3D printing, noise reduction, computational fluid dynamics

1 Introduction

In recent years, with the improvement of living standards and increased personal wealth, vehicle comfort has been of increasing concern. In cities within China demonstrating higher living standards, noise pollution grievances account for 60%~70%

of all pollution complaints. This is a social problem requiring urgent improvement. Hence, reducing vehicle noise has become a priority for major automobile manufacturers.

In the fierce competition of the automobile market, noise, vibration and harshness (NVH) performance is an important quality index of vehicle evaluation. Cooling system noise increases with increase in engine load and speed, and is identified as a primary noise source of road vehicles fitted with internal combustion engines. Currently, there are many potential solutions to reduce the noise of cooling fans. Traditional research has mainly focused on changes to the fan hub ratio, blade profile, blade installation angle and blade number[1,2] as outlined below.

Cattanei et al.[3] proposed a method for the reduction of tonal noise annoyance from axial flow fans based on uneven circumferential blade spacing. Their work demonstrated that they were able to reduce the tonal noise annoyance by optimal spacing of the fan blades. Further work by Corsini et al.[4] identified a measure to reduce fan noise by the introduction of profiled endplates at the blade tip that changed the tip leakage flow behavior. This research revealed that modifications to the tip geometry markedly affected the multiple vortex creation due to blade tip leakage flow leading to reduced fan noise.

Govardhan et al.[5] studied the influence of blade geometry on the flow rate of a cross-flow fan by using a three-impeller geometry with different blade angles and radius ratios. Krishna et al.[6] performed an experimental study on a low-noise baseline fan and compared its noise propensity against three alternative redesigned composite material fans. The experimental parameters under investigation were varied aerofoil-shape blade cross-section, the use of inlet bell-mouth entry, the use of composite materials, a reduction in the number of blades, the introduction of uneven blade spacing (as suggested by Cattanei et al.[3]) ensuring it to be a mixed flow fan, the use of backward-skewed blade design and the reduction of tip clearance. It is observed that a mixed flow fan consisting of seven evenly spaced blades with backward swept shape produced the low-noise fan design at the fan operating point.

Kamada et al.[7] employed an indirect noise prediction method to theoretically evaluate noise for blower units. This method was validated through a comparison with actual sound pressure level measurements. The results revealed that the sound pressure level of the blower unit can be reduced by decreasing the local flow velocity on the meridian plane due to a blockage factor, and a multi-blade fan with short chord length could achieve both high total pressure efficiency and low sound pressure level.

In the early research, the noise optimization of cooling fans was mainly studied

through experimental methods[8,9]. However, the emergence and development of CFD techniques provided greater opportunities to further extend this research[10,11].

Behzadmehr et al.[12] used the design of experiment (DOE) method and CFD calculations to analyze the sensitivity of entrance design parameters for a backward-inclined centrifugal fan. Hashim et al.[13] adapted the large eddy simulation (LES) model and the Ffowcs Williams-Hawkings (FW-H) model to simulate and analyze the velocity distribution near the fan blade area as well as the sound pressure distribution characteristics of different sections in the front and back drainage basins of the fan.

Krishna et al.[14] continued their work and studied the design of the motor fan as used on a submarine sea water pump motor. This work identified the noise source of the fan by using the commercial CFD package, FLUENT, and a computational air acoustic code, which led to a greater understanding of the overall sound pressure level of the fan and noise reduction from the motor fan.

At this point, the application of bionic structures to optimize acoustic performance of fan blades was in its infancy. However, the biological inspired approach has achieved many notable advances in many scientific research fields and practical projects. Bionic noise reduction techniques intend to analyze and study biological characteristics related

to drag and noise reduction in nature. The aim is to extract the principles and rules of nature and apply them to engineering practice as a means to achieve low noise characteristics as observed in similar bionic organisms[15~17]. Flying animals and marine creatures formed their unique biological designs through a long evolutionary process. As such, their body surfaces and profiles have the characteristics of low viscosity, friction reduction and consequential noise reduction. These excellent characteristics of biological surfaces and profiles provide a reference basis for biological inspired research and broadens the scope of such investigations [18~20].

This paper innovatively combines the biological inspired approach with automotive noise reduction in order to redesign the flow surface of cooling fan blades in accordance to the principles of nature. This novel work provides a new and feasible solution for the noise reduction of cooling fans.

2 Bio-inspired design and 3D printing

2.1 Design principle

Shark skin is a formation, or structure, of small shield scales where each individual shield scale exhibits a characteristic morphology of grooves and parallel ridges. In the swimming process, the ridge structure of the shield scales cuts against the direction of water flow to disturb the water flow near the shark's skin, and hence reduces the

turbulence and surface drag between the water flow and the shark skin. Another example of nature at its best may be seen within the fin structure of fish as illustrated in Figure 1. This shows a similar distribution of rigid bulges and flexible depressions, which can be simplified into a structure of alternating ridges and grooves. This "structure" controls the direction of fish when swimming and serves to direct the fluid flowing over the fish's body. Similarly, most shellfish have the familiar longitudinal structure on the shell surface formed by ribbed ridges and grooves that are evenly spaced – as shown in Figure 2. This design of nature optimises surface flow over the shell surface so delivering a reduced drag, avoiding unwanted migration, and a greater resistance to erosion and wear.

Figure 1. Fin configuration

Figure 2. The structure of shellfish

2.2 Bio-inspired design

After comparison of potential schemes, the bio-inspired structure selected in this paper comprises three ribbed ridges which are distribution concentric to the fan hub axis to direct air flow across the fan blade as shown in Figure 3. An orthogonal DOE scheme is designed with four factors and three levels as shown in Table 1. Figure 3 shows the radial position of the ribbed ridges to be factor A, the width of the ribbed ridges as factor B, the height of the ribbed ridges as factor C and the pitch distance between the ribbed ridges as factor D.

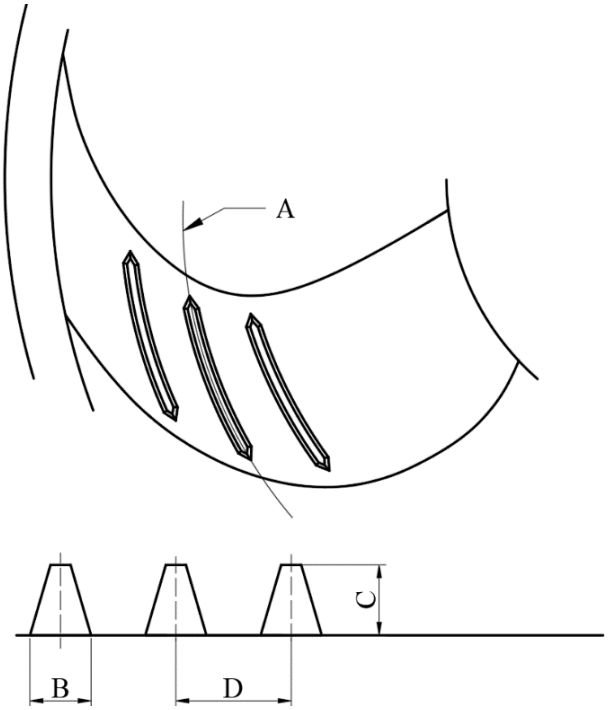

Figure 3. Schematic diagram of bio-inspired blade of cooling fan

Table 1. Orthogonal design factor and level of fan blade

Level \ Factor	A Radius position (mm)	B Ridge width (mm)	C Ridge height (mm)	D Ridge pitch distance (mm)
1	136	1	0.5	5
2	146	2	1	10
3	156	4	2	15

Each of the 4 factors have 3 levels with a permutation that provides 9 groups of plans leading to the orthogonal matrix of four factors and three levels, giving a total of 9 experiments according to DOE principles as shown in Table 2.

Table 2. Orthogonal designed experiments for fan blade structure

Design number \ Factor	A Radius position (mm)	B Ridge width (mm)	C Ridge height (mm)	D Ridge pitch distance (mm)
FA1	136	1	0.5	5
FA2	136	2	1	10
FA3	136	4	2	15
FA4	146	1	1	15
FA5	146	2	2	5
FA6	146	4	0.5	10
FA7	156	1	2	10
FA8	156	2	0.5	15
FA9	156	4	1	5

2.3 Fabrication

The manufacture of a bespoke fan blade can be expensive if conventional manufacturing techniques are employed. Two approaches could be adopted, one that produces the individual ribs that would then be adhered to the surface of a standard blade and a second that would create the blade with integral ribs as one piece. An initial observation of the rib dimensions suggests that the former choice would be a delicate operation but detachment at full fan speed may be an issue. As such, the second option was seen as the better choice. An additive manufacturing process known as 3D printing is well established and used extensively for creating complex experimental or prototype parts. This is a technique that "prints" increasing layers of material, one layer on top of another, each with a slightly differing profile, until a complete 3D model is created. The basic starting point is a 3D computer aided design (CAD) image as created for any design. It may be a solid or hollow object that represents the desired initial experimental design. It is important to understand that the construction material has to be sufficiently robust to withstand the real operating parameters demanded in addition to replicating the final design in every aspect.

For these investigations, the fan blades with the integrated bionic structures were manufactured using the 3D printing process with "Future 8000 resin", a polyimide high

heat-resistant resin, as shown in Figure 4.

(a) (b) (c)

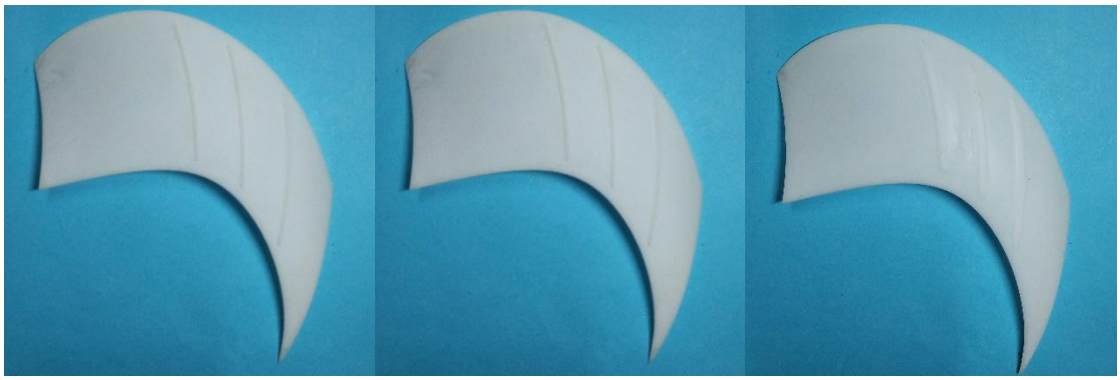

(d) (e) (f)

(g) (h) (i)

Figure 4. 3D printed sample of bio-inspired blade. (a) FA1; (b) FA2; (c) FA3; (d) FA4; (e) FA5; (f) FA6; (g) FA7; (h) FA8; (i) FA9

3 Experiment

3.1 Experimental methodology

(1) To monitor the fan speed, a reflective strip was attached to one of the original fan blades. This strip served to provide the return signal for a laser AR-926-non-contact tachometer. Having attached the strip it was necessary to calibrate the voltage/speed characteristics of the motor so that subsequent test speed settings could be determined using the motor voltage level. This method allowed the speed to be adjusted without fixing the reflective strip to the modified fan blades which could influence the airflow over the blades.

(2) The noise measurements were conducted in an acoustic free field environment within a semi-anechoic chamber with a solid ground and a background noise of no more than 45 dB(A). The fan was positioned according to the actual operational height with the sound pressure sensor (model INV9206 produced by China Orient Institute of Noise & Vibration) positioned at the same height, but 1 meter away from the fan outlet. The fan with the original blades was operated for 15 minutes before the sound pressure meter was used to measure the reference noise emissions. The sound pressure sensor reading was recorded by a data acquisition and signal processing (DASP) system. A laptop was used for subsequent analysis of the data. Figure 5 shows the schematic

diagram for the cooling fan noise tests.

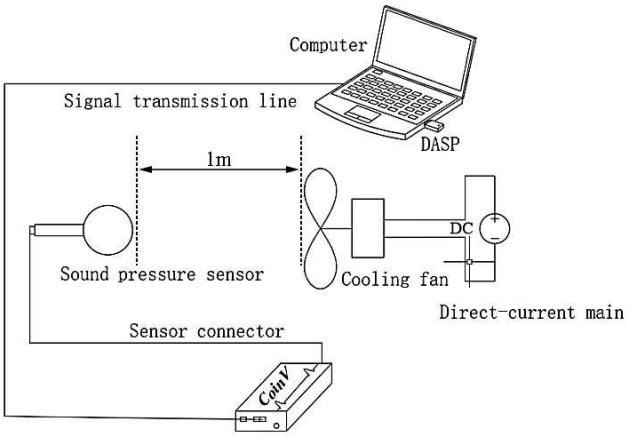

Figure 5. Schematic diagram of cooling fan noise test

(3) Having determined the baseline noise generated by the standard fan, the original fan blades were changed for the biomimetic structure blades and the assembly reinstalled within the semi-anechoic chamber. As with the original fan, all tests were preceded by running the fan for 15 minutes before measurements were recorded. For each blade design, the motor speed was adjusted from a low (1000 r/min) to high speed (2500 r/min) and the noise monitored at incremental speed settings of 250 r/min, giving 7 running speeds for each blade design. All tests were repeated 3 times under the same conditions to check for consistency. After each test, the collected data were correlated and analysed to give the standard A-weighted sound pressure level (SPL) in units of dB(A).

3.2 Experimental results

The average measured A-weighted noise levels of the 7-speed groups are shown in Table 3. FA0 is the reference design without the bio-inspired blades and FA1 to FA9 represent the bio-inspired fan designs as shown in Figure 4. In all cases, the speed ranges from 1000 r/min to 2500 r/min in incremental steps of 250 r/min.

Table 3. The average A-weighted noise levels in dB(A) for the different fan designs as a function of fan speed

Fan speed / Design number	1000 r/min	1250 r/min	1500 r/min	1750 r/min	2000 r/min	2250 r/min	2500 r/min
FA0	53	54.37	61.86	65.37	66.21	70.18	73.18
FA1	51.8	54.69	62.83	64.54	65.61	70.45	72.11
FA2	51.15	52.52	60.2	61.39	66.65	69.83	73.1
FA3	52.82	54.23	60.42	61.54	65.27	67.86	69.85
FA4	53.05	53.43	61.61	62.26	65.81	69.66	71.75
FA5	51.47	57.09	62.7	64.44	66.99	68.6	73.96
FA6	51.87	55.21	61.11	62.36	63.62	68.79	71.14
FA7	52.66	53.45	60.26	61.84	65.29	68.54	72.46
FA8	52.34	55.29	61.6	62.33	65.24	69.79	73.24
FA9	54.26	56.09	60.08	62.9	64.63	66.85	69.8

It can be seen from Table 3 that, in general, the measured SPL for the bio-inspired fan designs are lower than for the FA0 original design but the magnitude of this reduction is dependent on the fan speed. As an example, the SPL's of the bionic fans are

all lower than the reference fan at 1750 r/min as shown in Figure 6, with a maximum reduction of around 3.5 dB(A) for the designs FA2 and FA3.

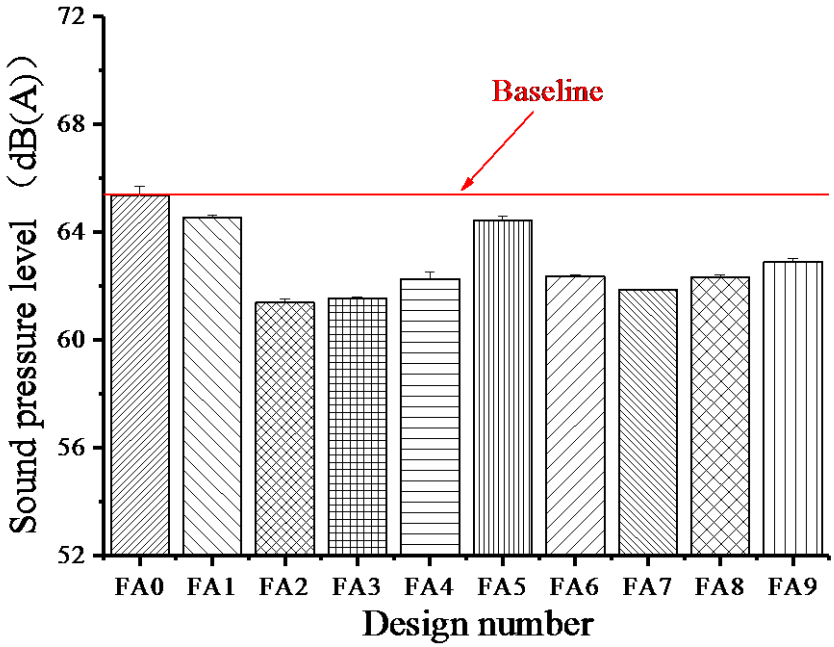

Figure 6. Sound pressure level of each fan design at 1750 r/min

As a means to determine the overall effectiveness of the individual designs, each design is awarded a rating of 1 for the best and 9 for the worst. The score for each design over the 7 speed ranges is averaged. Each design average is then normalized with respect to the overall average to identify the best designs. The general results are shown

in Figure 7, where the value of 1 indicates neutral or average score. A lower value is better than the average in terms of reducing the SPL and a higher value would be worse than the average. From this basic analysis, it is clear that the good bio-inspired designs for further investigation are FA2, FA3, FA6, FA7 and FA9.

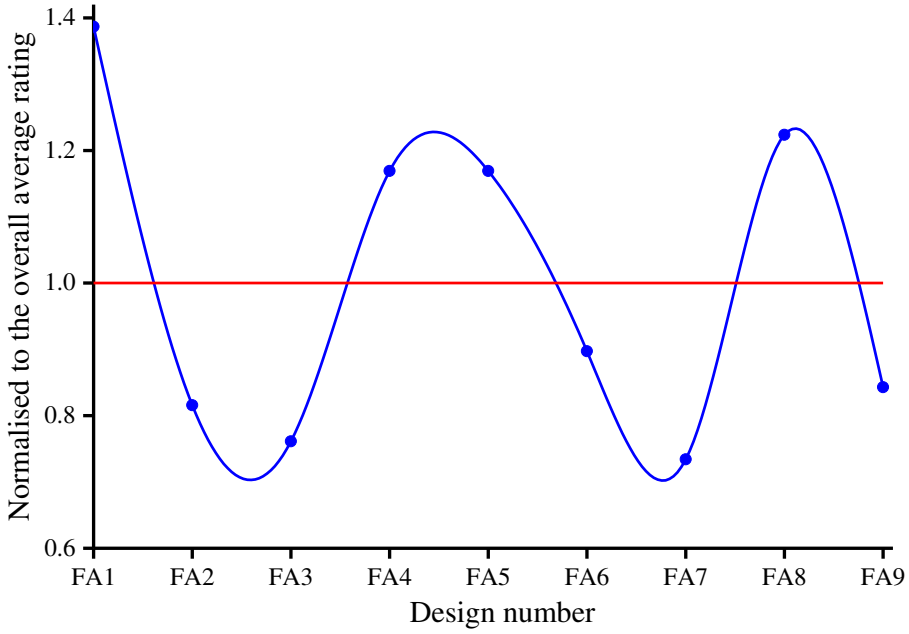

Figure 7. Average SPL for designs FA1-FA9 normalised to the overall average SPL

A further analysis would be to consider the effects of each design with regard to speed. The same rating method was used but a moving average was calculated over the 7 speed ranges for each design and normalized with respect to the average for the 9 designs at each speed. The results of this analysis are shown in Figure 8 which indicates that the best bio-inspired designs across the speed range are FA2, FA3, FA6, FA7 and FA9. It should be noted that design FA2 is clearly the better design at the lower speeds but becomes less effective above 1750 r/min.

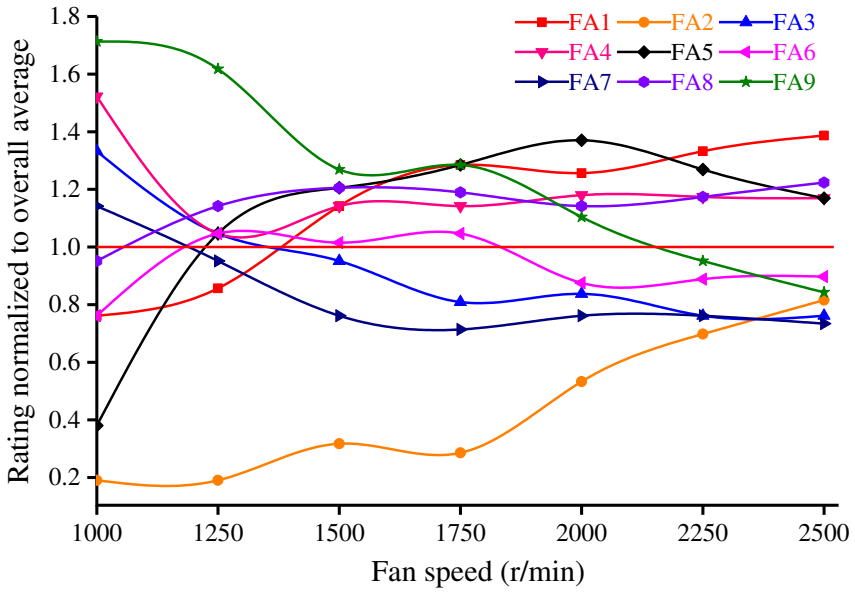

Figure 8. Moving average of each test SPL normalized with respect to the overall average SPL at each speed

In order to analyse the four factors of radial distance A, ridge width B, ridge height C, and ridge pitch distance D in the orthogonal DOE scheme, a variance analysis of the effect of each factor at the 7 rotating speeds was conducted, as shown in Table 4. In addition, the primary and secondary relationships of the three levels, corresponding to each factor, on the influence of cooling fan noise were also analysed.

In the analysis of variance, Fa is obtained through the F test critical value table[21], and F values calculated are compared to obtain the significance of each factor. In this paper, the significance is classified by a "*" rating, and the larger the quantity F, the higher the significance of the corresponding factor. According to Table 4, ridge width B is the most significant factor at the lowest rotational speed of 1000 r/min, followed by radial distance A. When the rotation speed is increased in the range from 1250 r/min to 1750 r/min, ridge distance D is the most significant factor, and at speeds of 2000 r/min to 2500 r/min, ridge width B becomes the most significant factor.

Table 4. Variance analysis of noise reduction effect at each rotation speed for the 4 design factors A-D

Rotation speed (r/min)	Source of variation	Sum of deviation square	DOF	Mean sum of square	F	Fa	Significance
1000	A	6.74	2	3.37	13.48	F0.01(2,9)=8.02	***
	B	8.01	2	4.01	16.04	F0.05(2,9)=4.26	***
	C	3.30	2	1.65	6.60		**
	D	4.16	2	2.08	8.32		***
	Error	4.51	18				
	SUM	26.72	26				
1250	A	10.17	2	5.09	36.36	F0.01(2,9)=8.02	***
	B	9.29	2	4.65	33.21	F0.05(2,9)=4.26	***
	C	5.93	2	2.97	21.21		***
	D	24.40	2	12.20	87.14		****
	Error	2.54	18				
	SUM	52.33	26				
1500	A	6.29	2	3.15	39.375	F0.01(2,9)=8.02	***
	B	6.12	2	3.06	38.25	F0.05(2,9)=4.26	***
	C	6.57	2	3.29	41.13		***
	D	8.06	2	4.03	50.38		****
	Error	1.49	18				
	SUM	28.53	26				
1750	A	3.17	2	1.59	22.71	F0.01(2,9)=8.02	***
	B	1.28	2	0.64	9.14	F0.05(2,9)=4.26	***
	C	3.04	2	1.52	21.71		***
	D	24.21	2	12.11	170.56		*****
	Error	1.28	18				
	SUM	32.98	26				
2000	A	2.83	2	1.42	17.75	F0.01(2,9)=8.02	***
	B	14.59	2	7.30	91.25	F0.05(2,9)=4.26	****
	C	5.62	2	2.81	35.13		***
	D	1.27	2	0.64	8.00		**
	Error	1.50	18				
	SUM	25.81	26				

Table 4. Variance analysis of noise reduction effect at each rotation speed for the 4 design factors A-D (con.)

Rotate speed (r/min)	Source of variation	Sum of deviation square	DOF	Mean sum of square	F	Fa	Significance
2250	A	4.24	2	2.12	12.47	F0.01(2,9)=8.02	***
	B	17.92	2	8.96	52.71	F0.05(2,9)=4.26	****
	C	8.62	2	4.31	25.35		***
	D	1.25	2	0.63	3.71		*
	Error	3.01	18				
	SUM	35.04	26				
2500	A	2.67	2	1.34	5.15	F0.01(2,9)=8.02	**
	B	41.79	2	20.90	80.38	F0.05(2,9)=4.26	****
	C	1.54	2	0.77	2.96		*
	D	5.95	2	2.98	11.46		***
	Error	4.69	18				
	SUM	56.64	26				

From the variance analysis of measured noise shown in Table 4, factor D (ridge pitch distance) has the most significant impact on noise reduction under low speed conditions whilst, under high speed conditions, factor B (ridge width) has the most significant influence. Large pitch distance (D) and short ridge width (B) have little effect on fan surface air flow since the fan blades are then almost smooth. Smaller ridge distance can hinder airflow and increase air resistance. Other factors (A, C) have little difference in reducing the noise of the cooling fan. Shark skin has a structure of small shield scales where each individual shield scale exhibits a characteristic morphology of grooves and parallel ridges, although this is not obvious from a distance. Here, the

optimal levels of pitch distance and ridge width appear to be 10 mm and 4 mm, respectively.

This result is confirmed by the significant observation from the noise tests that the most effective noise reduction designs (FA2, FA3, FA6, FA7) all possess a relatively higher ridge pitch distance (10 mm) and/or the greatest ridge width (4 mm).

4 Numerical Simulation

4.1 Governing equations

Theoretically, CFD is based on the governing equations of fluid dynamics. The physical phenomenon of fluid motion is the object of CFD analysis and prediction. After these physical equations are determined, they can be described as equations suitable for computational fluid dynamics.

4.1.1 Mass conservation equation

The law of conservation of mass is defined as follows: the increase of mass per unit time of a fluid microelement is equal to the net mass flowing into the microelement at the same time interval. This law gives rise to the following mass conservation equation:

$$\frac{\partial \rho}{\partial t} + div(\rho \vec{u}) = \frac{\partial \rho}{\partial t} + \frac{\partial (\rho u)}{\partial x} + \frac{\partial (\rho v)}{\partial y} + \frac{\partial (\rho w)}{\partial z} = 0 \tag{1}$$

Where ρ is density, t is time, $\vec{u}$ is velocity vector, u , v and w is the component of the velocity vector $\vec{u}$ in the x, y and z direction, respectively.

4.1.2 Momentum conservation equation

The law of conservation of momentum, which is a form of Newton's second law, is expressed as: the rate of change of momentum with respect to time in a microelement is equal to the sum of the forces acting on it by the outside world. This law gives rise to the following momentum conservation equations:

$$\frac{\partial(\rho u)}{\partial t}+div(\rho u\vec{u})=-\frac{\partial p}{\partial x}+\frac{\partial \tau_{xx}}{\partial x}+\frac{\partial \tau_{yx}}{\partial y}+\frac{\partial \tau_{zx}}{\partial z}+F_x \tag{2}$$

$$\frac{\partial(\rho v)}{\partial t}+div(\rho v\vec{u})=-\frac{\partial p}{\partial y}+\frac{\partial \tau_{xy}}{\partial x}+\frac{\partial \tau_{yy}}{\partial y}+\frac{\partial \tau_{zy}}{\partial z}+F_y \tag{3}$$

$$\frac{\partial(\rho w)}{\partial t}+div(\rho w\vec{u})=-\frac{\partial p}{\partial z}+\frac{\partial \tau_{xz}}{\partial x}+\frac{\partial \tau_{yz}}{\partial y}+\frac{\partial \tau_{zz}}{\partial z}+F_z \tag{4}$$

Where p is the pressure on a fluid microelement, τ_{xx} 、 τ_{xy} and τ_{xz} are components of viscous stress, F_x 、 F_y and F_z are volume forces on a small element.

Equations (2), (3), (4) apply for all fluids. For Newtonian fluids, since the viscous stress is proportional to the fluid deformation rate, the following equations can be derived:

$$\frac{\partial(\rho u)}{\partial t}+div(\rho u\vec{u})=div(\mu gradu)-\frac{\partial p}{\partial x}+S_u \tag{5}$$

$$\frac{\partial(\rho v)}{\partial t}+div(\rho v\vec{u})=div(\mu gradv)-\frac{\partial p}{\partial y}+S_v \tag{6}$$

$$\frac{\partial(\rho w)}{\partial t}+div(\rho w\vec{u})=div(\mu gradw)-\frac{\partial p}{\partial z}+S_w \tag{7}$$

Where S_u, S_v and S_w are generalized source term of momentum conservation equation, $S_u=F_x+\mathrm{s}_x$, $S_v=F_y+\mathrm{s}_y$ and $S_w=F_z+\mathrm{s}_z$. For incompressible fluids with constant viscosity, $\mathrm{s}_x=\mathrm{s}_y=\mathrm{s}_z=0$.

4.1.3 Energy conservation equation

The law of conservation of energy can be expressed as: the rate of increase in energy in a microelement is equal to the net heat flux into the microelement plus the work done on the microelement by the volume and surface forces. This law gives rise to the following energy conservation equation:

$$\frac{\partial(\rho \mathrm{T})}{\partial t}+div(\rho\vec{u}T)=\mathrm{div}(\frac{k}{c_p}gradT)+S_T \tag{8}$$

The expanded form of this equation is shown below:

$$\frac{\partial(\rho \mathrm{T})}{\partial t}+\frac{\partial(\rho u \mathrm{T})}{\partial x}+\frac{\partial(\rho v \mathrm{T})}{\partial y}+\frac{\partial(\rho w \mathrm{T})}{\partial z}=\frac{\partial}{\partial x}(\frac{k}{c_p}\frac{\partial T}{\partial x})+\frac{\partial}{\partial y}(\frac{k}{c_p}\frac{\partial T}{\partial y})+\frac{\partial}{\partial z}(\frac{k}{c_p}\frac{\partial T}{\partial z})+S_T \tag{9}$$

Where c_p is specific heat at constant pressure, T is temperature, k is heat transfer coefficient of fluid, S_T is viscous dissipation term.

4.1.4 Turbulence equation

Under turbulent flow, the direct calculation of the three - dimensional transient N-S equation is more demanding for computer operation. The transient N-S equation is averaged in most engineering applications. At the same time, the turbulence model equation reflecting the turbulence characteristics is supplemented, such as in the $k-\varepsilon$ turbulence model.

The equation of turbulent kinetic energy k is as follows:

$$\frac{\partial(\rho k)}{\partial t}+div(\rho\vec{u}k)=div\left[\left(\mu+\frac{\mu_t}{\sigma_k}\right)\cdot gradk\right]-\rho\varepsilon+\mu_t P_G \tag{10}$$

The equation of turbulence dissipation rate ε is as follows:

$$\frac{\partial(\rho\varepsilon)}{\partial t}+div(\rho\vec{u}\varepsilon)=div\left[\left(\mu+\frac{\mu_t}{\sigma_\varepsilon}\right)\cdot grad\varepsilon\right]-\rho C_2\frac{\varepsilon^2}{k}+\mu_t C_1\frac{\varepsilon}{k}P_G \tag{11}$$

Where $P_G=2\left[\left(\frac{\partial u}{\partial x}\right)^2+\left(\frac{\partial v}{\partial y}\right)^2+\left(\frac{\partial w}{\partial z}\right)^2\right]+\left(\frac{\partial u}{\partial y}+\frac{\partial v}{\partial x}\right)^2+\left(\frac{\partial u}{\partial z}+\frac{\partial w}{\partial x}\right)^2+\left(\frac{\partial v}{\partial z}+\frac{\partial w}{\partial y}\right)^2$,

C_μ, σ_k, σ_ε, C_1, C_2 are constant, $\mu_t=\rho C_\mu\frac{k^2}{\varepsilon}$.

To facilitate the analysis and solution of the governing equation, ϕ is used as a universal variable to give the general form as follows:

$$\frac{\partial(\rho\phi)}{\partial t}+div(\rho\vec{u}\phi)=div(\Gamma\cdot grad\phi)+S \tag{12}$$

The expanded form of this equation is shown below:

$$\frac{\partial(\rho\phi)}{\partial t}+\frac{\partial(\rho u\phi)}{\partial x}+\frac{\partial(\rho v\phi)}{\partial y}+\frac{\partial(\rho w\phi)}{\partial z}=\frac{\partial}{\partial x}\left(\Gamma\frac{\partial\phi}{\partial x}\right)+\frac{\partial}{\partial y}\left(\Gamma\frac{\partial\phi}{\partial y}\right)+\frac{\partial}{\partial z}\left(\Gamma\frac{\partial\phi}{\partial z}\right)+S \qquad (13)$$

Where ϕ is universal variable, Γ is generalized diffusion coefficient, S is generalized source term.

4.2 CFD modelling

The standard axial cooling fan with a diameter of 387 mm was taken as the prototype, as shown in Figure 9, and the three-dimensional model of the fan was created using SOLIDWORKS. In order to reduce the calculation time, the complex hub hole structure and rounded corners were simplified, as shown in Figure 10. FA0 and FA3 were selected as suitable designs for comparative simulation analysis, FA3 being identified as the most promising bio-inspired design strategy to pursue. The bionic ridge structure of the orthogonal scheme FA3 is also convenient for mesh generation and simulation calculation so it is a good representative design and includes the most promising design features.

Figure 9. The standard axial cooling fan

According to the requirements of the fan performance CFD simulation, the whole simulation model is divided into four regions. These are the rotating fluid region (i.e. the fan itself), the channel region between the rotating fan and the fixed casing, the fan inlet region and the outlet region, as shown in Figure 10. According to the requirements for flow stability[22], the length of the inlet region should be 6 times the fan diameter and was therefore set to 2500 mm, and the length of the outlet region should be 10 times the fan diameter and was therefore set to 4100 mm. As shown in Figure 11, according to the design of the actual fan, the outer diameter of the fan rotor is 5 mm away from the fixed outer frame. As a result, the radial distance between the channel region and the rotating fluid region was set to 5 mm.

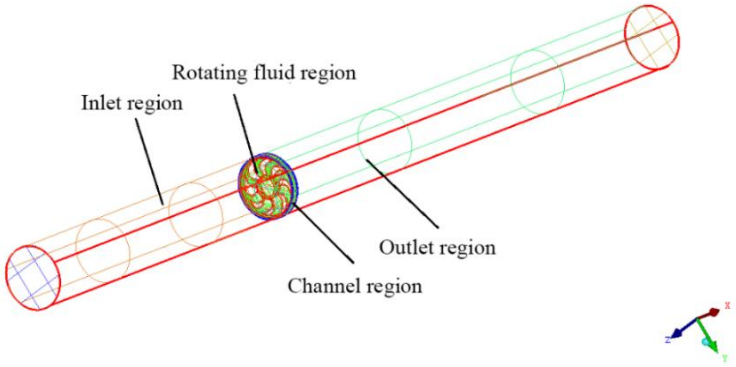

Figure 10. CFD simulation domain division of cooling fan

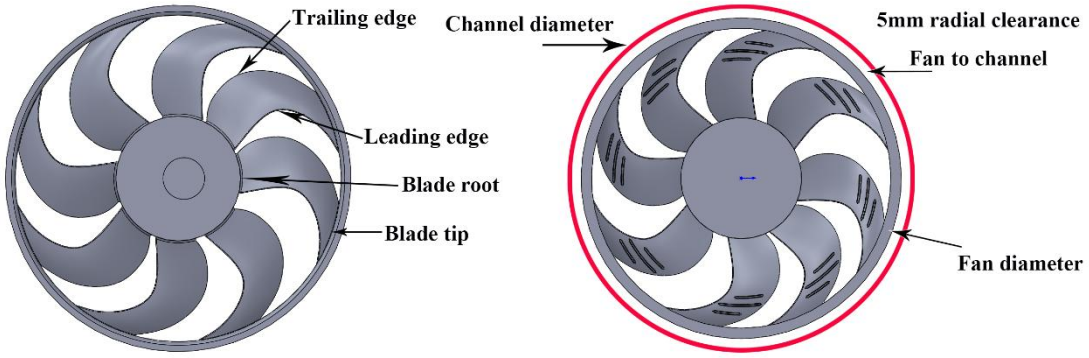

(a) (b)

Figure 11. Simplified cooling fan model. (a) FA0; (b) FA3

The mesh density is the aspect of CFD analysis which determines the accuracy and efficiency of the calculations. All the solutions obtained by CFD are approximate solutions. Too sparse a mesh will lead to too large an error in the results, and too dense a mesh will lead to an unnecessary increased demand for computing resources/power.

Therefore, under the premise of considering the complex surface of fans, the mesh density should be adopted to ensure the accuracy of simulation calculation and reduce the calculation demand whilst meeting the computational requirements. In this paper, ICEM CFD (integrated computer engineering and manufacturing code for computational fluid dynamics) is used to divide the whole fluid domain into an optimum mesh. A structured mesh was used in the inlet and outlet regions, with a relatively low mesh density, whereas an unstructured mesh was used in both the rotating fluid region and channel region with a relatively high mesh density. Three prismatic layers were set on the surface of the fan. The specific mesh types, mesh sizes, and number of elements are shown in Table 5. The fan surface mesh distributions and the element quality histogram (range 0~1) of the fan as output by the ICEM software are shown in Figure 12. The X-axis of the histogram represents the quality range of the mesh, where 1 represents the most ideal mesh and 0 represents the worst quality mesh, and the Y-axis represents the number of elements in each quality range.

Table 5. Mesh property of simulation region

Region name	Mesh type	Mesh size	Number of elements
Rotating fluid region	Unstructured	5 mm	1.45 million
Channel region	Unstructured	8 mm	0.34 million
Inlet region	Structured	20 mm	0.7 million
Outlet region	Structured	14 mm	1.74 million

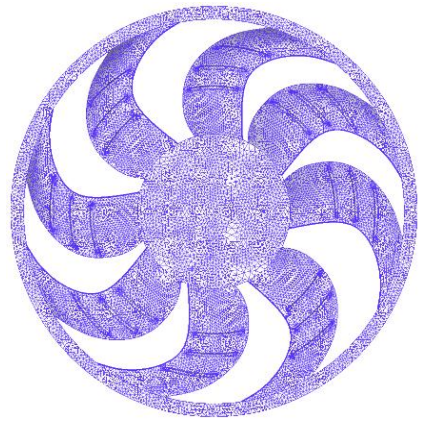

(a)

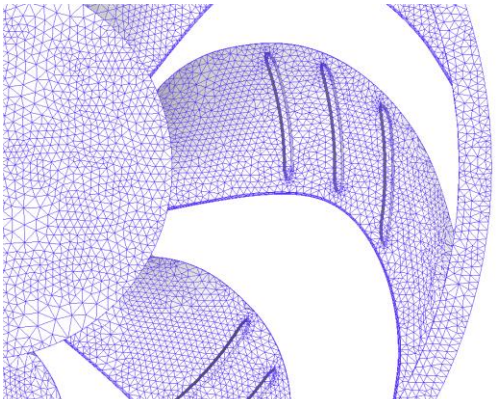

(b)

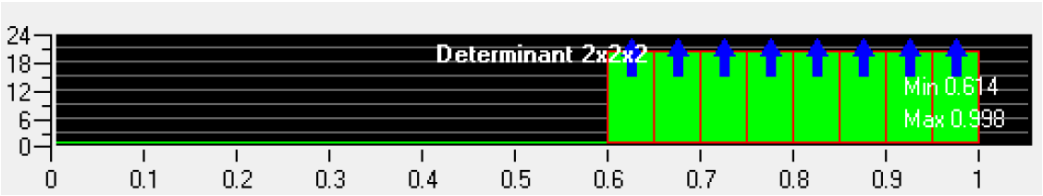

(c)

Figure 12. Mesh distribution of fan surface. (a) the whole mesh model; (b) the partial mesh model; (c) the element quality histogram of the fan

4.3 Simulation results and discussion

4.3.1 Blade surface velocity characteristics

On the suction (inflow) surface of the cooling fan, the velocity at the leading edge is relatively high in the region where the fan blade is in positive contact with the airflow. This initial high speed zone is followed by a low speed zone that extends to the middle of the fan blade but then the air again enters an increased velocity zone from the middle of the blade to the trailing edge. It should be noted that the blade root position is close to the hub and the tip position is close to the rotation ring, and as they are near to the curved junctions with these solid surfaces, both regions will experience some airflow obstruction. The airflow at the blade tip is also affected by the blade fixture ring and air centrifugal forces which result in this region exhibiting maximum surface velocity during fan operation, as shown in Figure 13 (a). In the presence of the bionic ridge structure, the flow velocity on the surface of fan blade is disturbed and the velocity decreases significantly at the leading end of the ridge structure. It is typically seen that, for the areas with the most increased airflow disturbance, the velocity at the trailing edge of the fan blade tip also decreases. In the velocity distribution diagram, it can be clearly seen from Figure 13 (b) that the overall surface velocity of the fan with the bionic ridge structure FA3 is lower than the prototype fan FA0.

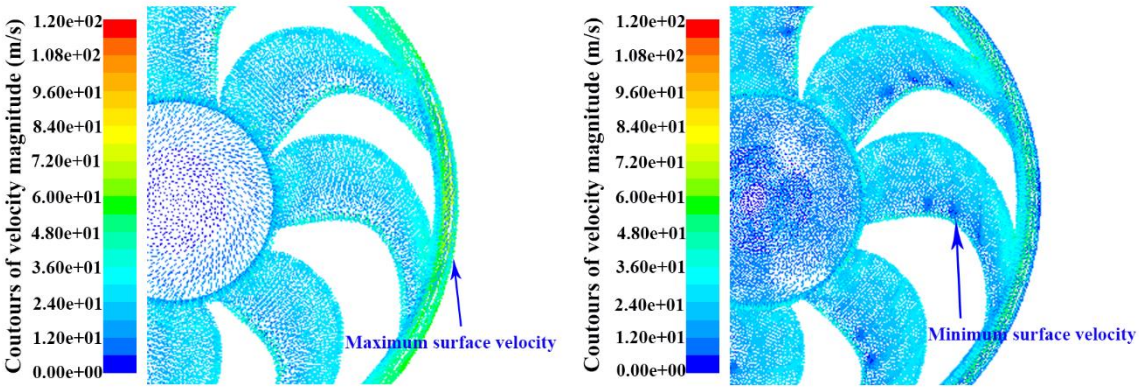

(a) (b)

Figure 13. Velocity distribution on the fan surface. (a) FA0; (b) FA3

4.3.2 Blade surface pressure characteristics

The dynamic pressure distributions of the cooling fans are shown in Figure 14. The dynamic pressure increases gradually from the leading edge to the trailing edge of the blade, and the dynamic pressure increases most significantly at the tip of the trailing edge. The difference of the dynamic pressure distribution on the surface of the blade between FA0 and FA3 is because the existence of the ridged structure makes the equivalent dynamic pressure area of the blade discontinuous. In Figure 14, it can be observed that the pressure area inside the ridged structure is extended, while on the corresponding outer side it is reduced.

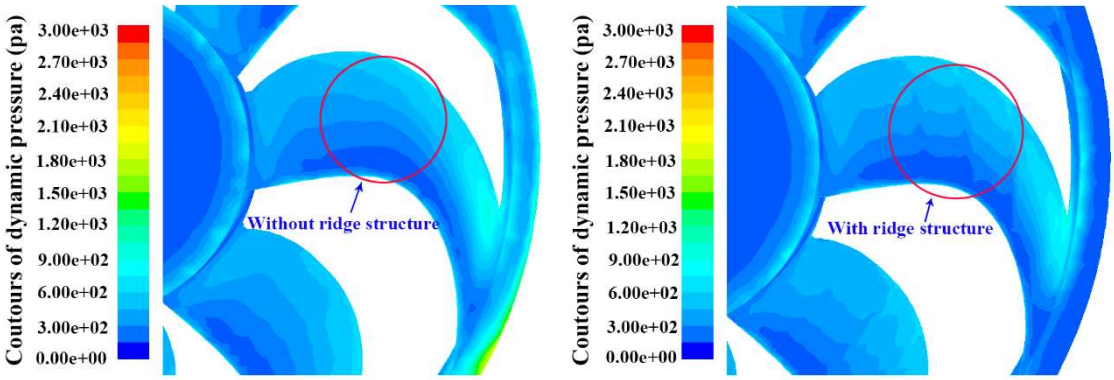

(a) (b)

Figure 14. Dynamic pressure distribution on the fan surface. (a) FA0; (b) FA3

The static pressure distributions on the surfaces of the cooling fans are shown in Figure 15(a) for the original design and Figure 15(b) for the FA3 bionic design. For both designs, the static pressures are positive in the areas where the blades are in direct contact with the airflow, while in other areas the static pressures are mainly negative. The negative pressure increases where the curvature of the blade surface increases and air speed is the greatest, and reaches a maximum at the blade tip near the trailing edge. From Figure 15(b), the existence of the ridge structure on the surface of the fan blade divides the static pressure area into identifiable regions. It can be seen that the absolute value of negative static pressure is at the same position for the basic fan design (FA0) but is lower. As such, it is suggested that the biomimetic structure reduces the absolute value of static pressure on the surfaces. In Figure 15(a), there is a large triangular blue area at the tip (indicated) which has the largest negative value of static pressure. The

corresponding blue area for the FA3 design in Figure 15(b) is clearly smaller which indicates an increase in air speed at this point.

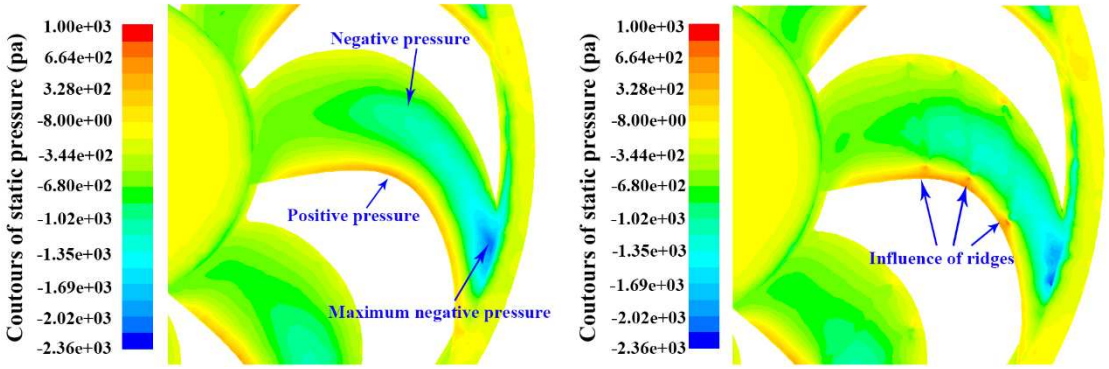

(a) (b)

Figure 15. Static pressure distribution on the fan surface. (a) FA0; (b) FA3

According to the dynamic and static pressure distributions on the surfaces of the cooling fan blades described above, it can be concluded that the total pressure in the blade tip area of the bionic cooling fan definitely reduces and the pressure at the trailing edge of the blade increases slightly. In addition, it is seen that the bionic ridge structure reduces fluid flow attachment to the smooth blade surface. The small horseshoe vortex generated by the ridge structure disturbs the fluid boundary layer, delays the transition of the laminar flow into the turbulence regime and reduces the intensity of the fan blade trailing edge vortex.

4.3.3 Turbulent kinetic energy and noise characteristics of blades

In fluid dynamics, turbulence kinetic energy (TKE) is the mean kinetic energy per unit mass associated with eddies in a turbulent flow. Physically, the TKE is characterized by measured Root-Mean-Square (RMS) velocity fluctuations. In the Reynolds-averaged Navier Stokes equations, the turbulence kinetic energy can be calculated based on the closure method, i.e. a turbulence model. Generally, the TKE can be quantified by the mean of the turbulence normal stresses.

Turbulent kinetic energy distributions of the original and modified cooling fans are shown in Figure 16. On the suction surface, the turbulent kinetic energy from the inside of the front side to rear tip shows an increasing discontinuous distribution, and reaches a maximum value at the trailing tip. Because of the curvature of the fan blade in the area near the blade tip, the fluid flow is more likely to be turning, generating secondary vortices near the fan edge and causing vortex noise. In Figure 16 (b), the presence of bionic ridge structure significantly reduces the area of the maximum turbulent kinetic energy near the trailing edge of the blade tip, and the position of maximum turbulent kinetic energy slightly moves forward, which is conducive to reducing the formation of secondary vortices. At the junction between the blade tip and the rotating ring, the geometry varies greatly, and the vortex strength in this region is larger than that in the

rest of the trailing edge. In addition, the rotating ring also greatly reduces the size of tip vortices of the modified cooling fan, which is conducive to the reduction of vortex noise.

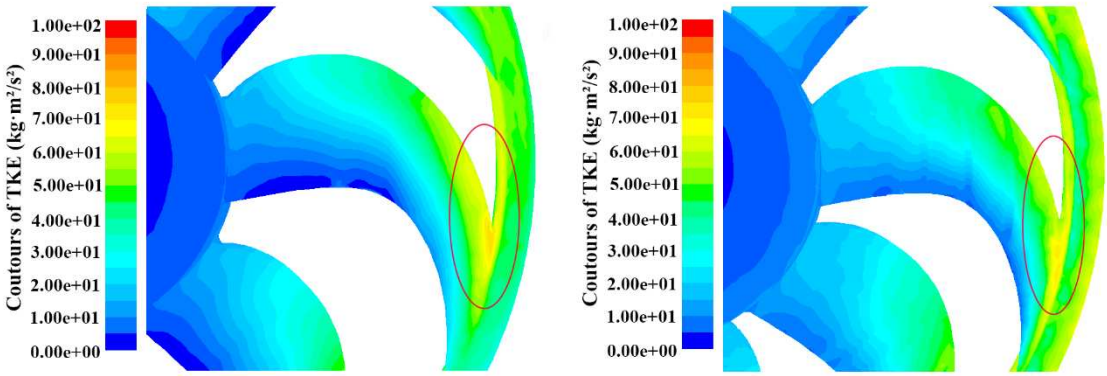

(a) (b)

Figure 16. Distribution of turbulent kinetic energy on the fan surface. (a) FA0; (b) FA3

The predicted aerodynamic noise level on the fan surface is shown in Figure 17 for the original and modified fans. In both cases, the noise generation is least at the leading edge, and greater at the trailing edge of the blade tip where the turbulent kinetic energy intensity is larger. By comparing Figure 17 (a) with Figure 17 (b), it can be seen that the presence of the bionic ridge structure has an impact on the noise level on the fan blade surface, mainly because the bionic structure reduces the fluid flow attachment in the

boundary layer, and thereby reduces the stability of the fluid closest to the blade surface. However, the main noise source of both cooling fans is the aerodynamic noise in the domain, which is caused by the pressure pulsation due to the fluid flowing through the running fan. Because of the existence of the ridge structure, the fluid within the boundary layer for the modified design is disturbed. The ridge structure is equivalent to a "vortex generator", producing small horseshoe vortices, and the direction of fluid velocity is different, thereby disturbing the fluid boundary layer, reducing the intensity of the boundary layer flow and delaying the transition point where the laminar flow transforms into turbulence. Both the intensity of gas vortex shedding and the level of aerodynamic noise in the basin are reduced by the modified design.

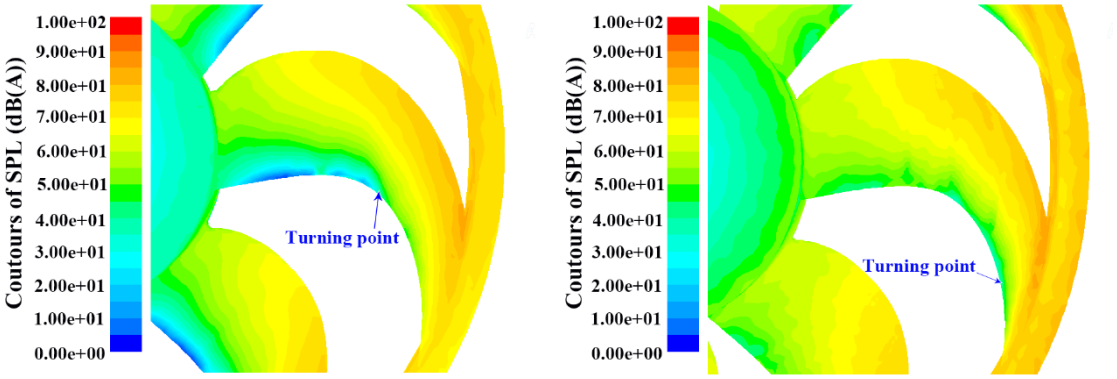

(a) (b)

Figure 17. Noise distribution on the fan surface. (a) FA0; (b) FA3

In Figure 18, the SPL is plotted with respect to the axis of the CFD domain from the sound field simulation of the cooling fan, so that the simulation and experiment can be compared with each other. The noise of the original cooling fan (FA0) at a position 1.0 m from the fan outlet region is 64.2 dB(A), while the experimental value is 73.18 dB(A). The noise of the cooling fan (FA3) at a position 1.0 m from the outlet region is 61.2 dB(A), while the experimental value at this position is 69.85 dB(A). Potential reasons for the discrepancies between the simulation and experiment are as follows: (1) in order to facilitate grid division and calculation, the CFD model of the cooling fan is simplified; (2) rotor vibration during fan operation is not considered in the simulation; and (3) even though noise testing of cooling fan is carried out in the semi-anechoic chamber, there may still be some influence of background environmental noise, while the simulation has no environmental noise at all. Given these factors, the agreement between simulation and test is reasonable and both show that the fan with the FA3 design of bio-inspired blades has a significantly lower noise signature.

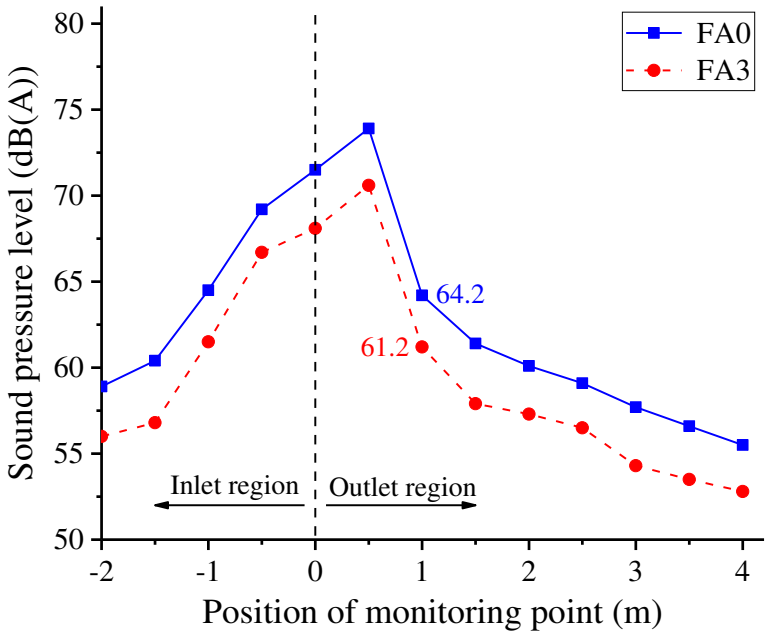

Figure 18. Variation of SPL with position of monitoring point

5 Conclusions

In this paper, reduction of noise from an automotive axial flow cooling fan was taken as the research objective. Bio-inspired structures with different ridged shapes for the fan blade surface have been designed as a potential way to reduce fan noise. The influence of the bio-inspired blade design on noise reduction of the cooling fan was investigated by means of both experimental and numerical analysis. The main conclusions are outlined below.

(1) Through the analysis of the experimental results, the noise reduction effect of the bio-inspired surface textures on the cooling fan blades was seen to be more significant with increase of rotational speed. The noise reduction effect of the bio-inspired design FA3 was the most significant in the speed range from 1500 r/min to 2500 r/min. At 1750 r/min, all the bio-inspired schemes reduced noise and, for example, the sound pressure level of the FA3 design was reduced by 3.83 dB(A) compared with the original design FA0.

(2) The simulation results show that the existence of the bio-inspired ridge structure on the blade surface is similar to that of a "vortex generator". The horseshoe-shaped vortices have an impact on the blade surface boundary layer, reducing the turbulent kinetic energy and delaying the transition of laminar flow to turbulence, the effect being to reduce the generation of fan blade trailing edge vortices leading to reduced aerodynamic noise.

(3) To reduce aerodynamic fan noise, there is a need to control the airflow over the fan blades through designs based on natural features leading to the concept of a bio-inspired design. The introduction of raised areas (ridges) with specific geometric characteristics such as size and spacing has been shown to be an effective way to reduce fan noise. Through variance analysis of the measured noise, the ridge pitch distance has

been found to have the most significant impact on noise reduction under lower speed conditions whilst the ridge width has the most significant influence at higher speeds.

Declaration of conflicting interests

The author(s) declared no potential conflicts of interest with respect to the research, authorship, and/or publication of this article.

References

1. Hu X, Wen S, Gao Y, et al. Experimental study on the effect of the shroud on the performance and flow field of an automotive cooling fan. *Proceedings of the Institution of Mechanical Engineers, Part D: Journal of Automobile Engineering* 2011; 225(5):627-642.
2. Wen S, Hao Y, Zhang Z, et al. Experimental study on the effect of different components collocations on flow of automotive cooling fan. *Proceedings of the Institution of Mechanical Engineers, Part D: Journal of Automobile Engineering* 2020; 234(1):270-282.

3. Cattanei A, Ghio R and Bongiovi A. Reduction of the tonal noise annoyance of axial flow fans by means of optimal blade spacing. *Applied Acoustics* 2007; 68(11-12):1323-1345.

4. Corsini A, Rispoli F and Sheard A.G. Development of improved blade tip endplate concepts for low-noise operation in industrial fans. *Proceedings of the Institution of Mechanical Engineers, Part A: Journal of Power and Energy* 2007; 221(5):669-681.

5. Govardhan M and Sampat D. Computational studies of flow through cross flow fans-effect of blade geometry. *Journal of Thermal Science* 2005; 14(3):220-229.

6. Krishna S, Krishna A and Ramji K. An experimental study on the reduction of motor-fan noise by modification of the blade and shroud configuration. *Proceedings of the Institution of Mechanical Engineers, Part C: Journal of Mechanical Engineering Science* 2010; 224(2):315-320.

7. Kamada M, Shimoyama K, Sato F, et al. Multi-objective design optimization of a high efficiency and low noise blower unit of a car air-conditioner. *Proceedings of the Institution of Mechanical Engineers, Part D: Journal of Automobile Engineering* 2019; 233(13):3493-3503.

8. Filios A, Tachos N, Fragias A, et al. Broadband noise radiation analysis for an HAWT rotor. *Renewable Energy* 2007; 32(9):1497-1510.

9. Tandon N. Noise-reducing designs of machines and structures. *Sadhana - Academy Proceedings in Engineering Sciences* 2000; 25(3):331-339.

10. Zuo S, Xie C, Wu X, et al. Numerical simulation and optimization of aerodynamic noise for claw pole alternator. *Proceedings of the Institution of Mechanical Engineers, Part C: Journal of Mechanical Engineering Science* 2019; 233(3):857-879.

11. Savory E, Martinuzzi R and Ryval J, et al. Evaluation of the thermofluid performance of an automotive engine cooling-fan system motor. *Proceedings of the Institution of Mechanical Engineers, Part D: Journal of Automobile Engineering* 2011; 225(1):74-89.

12. Behzadmehr A, Mercadier Y and Galanis N. Sensitivity analysis of entrance design parameters of a backward-inclined centrifugal fan using DOE method and CFD calculations. *Journal of Fluids Engineering* 2006; 128(3):446-453.

13. Hashim H M, Dogruoz M B and Arik M. Acoustic analysis of an axial fan. *2017 16th IEEE Intersociety Conference on Thermal and Thermomechanical Phenomena in Electronic Systems; 2017: IEEE*.

14. Krishna S, Krishna A and Ramji K. Reduction of motor fan noise using CFD and CAA simulations. *Applied Acoustics* 2011; 72(12):982-992.

15. Chen K, Liu Q, Liao G, et al. The sound suppression characteristics of wing feather of owl (Bubo bubo). *Journal of Bionic Engineering* 2012; 9(2):192-199.

16. Jung Y and Bhushan B. Wetting behavior of water and oil droplets in three-phase interfaces for hydrophobicity/philicity and oleophobicity/philicity. *Langmuir* 2009; 25(24):14165-14173.

17. Tian X, Han Z, Li X, et al. Biological coupling anti-wear properties of three typical molluscan shells—Scapharca subcrenata, Rapana venosa and Acanthochiton rubrolineatus. *Science China Technological Sciences* 2010; 53(11):2905-2913.

18. Bhushan B. Biomimetics: lessons from nature–an overview. *Philosophical Transactions of the Royal Society A: Mathematical, Physical and Engineering Sciences* 2009; 367:1445–1486.

19. García-Serna J, Pérez-Barrigón L and Cocero M.J. New trends for design towards sustainability in chemical engineering: Green engineering. *Chemical Engineering Journal* 2007; 133(1-3):7-30.

20. Ren L. Progress in the bionic study on anti-adhesion and resistance reduction of terrain machines. *Science in China, Series E: Technological Sciences* 2009; 52(2):273-284.

21. Ju S, Yan C, Wang X, et al. Effect of energy addition parameters upon scramjet

nozzle performances based on the variance analysis method. *Aerospace Science and Technology* 2017; 70:511-519.

22. Valencia E, Hidalgo V, Nalianda D, et al. Discretized Miller approach to assess effects on boundary layer ingestion induced distortion. *Chinese Journal of Aeronautics* 2017; 30(1):235-248.

APPENDIX

Notation

FA	3D printed sample of bio-inspired blade
A	Radius position
B	Ridge width
C	Ridge height
D	Ridge pitch distance
ρ	Density

t	Time
$\vec{u}$	Velocity vector
u , v and w	Component of the velocity vector $\vec{u}$ in the x, y and z direction
p	Pressure on a fluid microelement
τ_{xx} 、 τ_{xy} and τ_{xz}	Components of viscous stress
F_x 、 F_y and F_z	Volume force on a small element
S_u , S_v and S_w	Generalized source term of momentum conservation equation
c_p	Specific heat at constant pressure
T	Temperature
k	Heat transfer coefficient of fluid
S_T	Viscous dissipation term
ϕ	Universal variable
Γ	Generalized diffusion coefficient
S	Generalized source term